Optically Transparent Beam-Steering Reflectarray Antennas Based on a Liquid Crystal for Millimeter-Wave Applications

Aghabeyki, Peyman; Rosa, Pablo; Caño-García, Manuel; Quintana, Xabier; Guirado, Robert; Zhang, Shuai

Published in:
I E E E Transactions on Antennas and Propagation

DOI (link to publication from Publisher):
10.1109/TAP.2023.3332473

Publication date:
2024

Document Version
Accepted author manuscript, peer reviewed version

Citation for published version (APA):
Aghabeyki, P., Rosa, P., Caño-García, M., Quintana, X., Guirado, R., & Zhang, S. (2024). Optically Transparent Beam-Steering Reflectarray Antennas Based on a Liquid Crystal for Millimeter-Wave Applications. *I E E E Transactions on Antennas and Propagation*, *72*(1), 614-627. https://doi.org/10.1109/TAP.2023.3332473

Optically Transparent Beam-Steering Reflectarray Antennas Based on Liquid Crystal for Millimeter-Wave Applications

Peyman Aghabeyki, *Graduate Student Member*, *IEEE*, Pablo de la Rosa, Manuel Caño-García, Xabier Quintana, Robert Guirado, and Shuai Zhang, *Senior Member*, *IEEE*

Abstract*— This study presents a method to realize an optically transparent beam-steering antenna. The RF and optical features of Liquid Crystal (LC) technology are used in combination with transparent metal mesh to realize the first optically transparent reconfigurable reflectarray (RA). Since the electric field of bias and Radio Frequency (RF) signals are highly non-uniform, the LC permittivity is both anisotropic and inhomogeneous thus the behavior of LC molecules needs to be obtained for accurate modeling prior to antenna design. A unit cell consisting of metallic mesh and LC is analyzed and LC director distribution is obtained. The director data are transformed into permittivity tensors in the entire LC volume and the LC is discretized in electromagnetic simulation software to perform full-wave periodic boundary simulation to model the anisotropy and inhomogeneity. The discretized model is approximated by a single dielectric block with a new permittivity range for GT7 LC material. A 10×10 RA is fabricated and measured in terms of optical and RF performance. The measured phase shift of the unit cell is 260° when the voltage is increased from 0 V to 40 V. The measured beam scans from -10° to 50° in the E-plane and from -50 to +50 in the H-plane with a 14.35 dBi maximum gain. The prototype optical performance is also measured. The benefits and drawbacks of current RF LC mixtures are discussed. It shows that with an appropriate LC mixture optimized for both RF and optical transmission, the LC-based optically transparent antennas are a viable solution for various new applications.

***Index Terms*— Beam-Steering, optical transparent, Reflectarray, Liquid Crystal, Metallic Mesh, Transparent Antennas.**

I. INTRODUCTION

BEAM-STEERING antennas are an integral part of recent and future communication systems in millimeter waves. Over the years, a wide variety of technologies have been exploited to integrate beam-steering into antennas. Specifically, in reflectarrays (RA) and transmitarrays (TA), different techniques such as Pin diodes, varactor diodes, and Liquid Crystals (LC) are used to achieve beam steering and dynamic control of the antenna beam [1]. On the other hand, applying the concept of beam-steering in different applications such as mobile phones, radars, satellites, etc. requires a wide variety of standards and features depending on the cost, agility, performance, etc. Transparent antennas could be one of these applications.

Optically transparent antennas gained a lot of interest in recent years. In some applications, optical transparency will have a significant advantage. The fixed-beam transparent reflectarrays have been investigated over the recent years and also in [2] and [3] for solar panel integration. The reconfigurable RA can be used in the same scenario to provide beam-steering capability and improve the communication system. Moreover, the transparent beam-steering RA can be used as a Reconfigurable Intelligent Surface (RIS) in places that it benefits the transparency such as windows, glass walls in shopping centers where most of the walls are made of glass, etc.

Two of the main approaches to realizing transparent antennas are using Transparent Conductive Oxides (TCO) [4] and metal mesh [4]. Several works have addressed transparent fixed-beam RAs based on TCO [2][3] in which the rectangular patch unit cell is realized with Indium Tin Oxide (ITO). On the other hand, metal mesh structures also attracted significant attention over the years, and they have found their place in many applications. As for basic antenna structures, in [5], a microstrip patch is realized with a metal mesh structure for the ground plane and the patch for 2.5 GHz both in the form of Wire Metal Mesh (WMM) and Metal Mesh Film (MMF). In more complicated scenarios, a metal mesh structure is investigated in [6] that can be integrated with the phone's Liquid Crystal Display (LCD) screen. In [7], the authors proposed a metal mesh unit cell with a movable substrate to change the transmission coefficient of the unit cell at 28 GHz and realize a surface capable of controlling the transmission and reflection magnitude. By using this concept, they demonstrated a lens with dynamic switching between single and double focus. A multi-fixed-beam TA based on metal

Manuscript received XXX 2023; revised XXX 2023; accepted XXX 2023. (Corresponding author: Shuai Zhang.)

Peyman Aghabeyki and Shuai Zhang are with the Department of Electronic Systems, Aalborg University, 9220 Aalborg, Denmark (e-mail: sz@es.aau.dk)

P. de la Rosa is with the CEMDATIC and GEA, ETSI Telecomunicacion, Universidad Politecnica de Madrid, E-28040 Madrid, Spain.

Robert Guirado is with the Group of Applied Electromagnetism (GEA), ETSI Telecomunicación, Universidad Politécnica de Madrid, 28040 Madrid, Spain.

Manuel Caño-García and Xabier Quintana is with CEMDATIC, ETSI Telecomunicación, Universidad Politécnica de Madrid, 28040 Madrid, Spain.

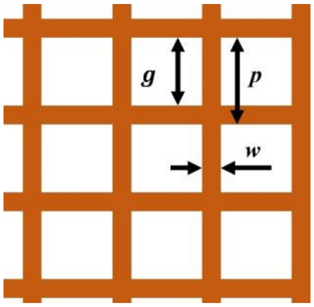

Fig. 1. Metal mesh structure and design parameters.

mesh is proposed in [8] in which a multilayer mesh ring patch on polymethylmethacrylate substrate is used to realize the TA structure that is optically transparent. However, there is still a lack of a fully integrated beam-steering mechanism in the literature.

Among different techniques that enable antenna beam-steering, Liquid Crystal (LC) is a promising technology due to its low cost, low power consumption, and limitless operating frequency. Over the years, LC technology has found its way from optics to microwave and millimeter waves. It has been used both in phased array antennas [9][10] as well as RAs [11][12] and it has been demonstrated to be a feasible solution for 2D beam-steering. However, to the best of our knowledge, there has been no report of optically transparent and fully reconfigurable beam-steering RA, or antenna and this problem remains unaddressed. In this work, we have investigated the possibility of leveraging the liquid crystal features, such as transparency and dielectric anisotropy, and applying that to optically transparent conductive metal mesh structures and realize for the first time, an optically transparent beam-steering antenna. Due to the low metal area of conductive mesh and non-uniform electric bias field, the unknown behavior of the LC is first characterized and then it is applied to the final antenna design.

The rest of the paper is organized as follows. Section II introduces the proposed unit cell modeling in the case of transparency and LC behavior. Section III discussed the modeling of RA by using an approximate model of the proposed unit cell. The entire fabrication process of LC-based transparent RA is presented in Section IV. The optical measurement results of the RA are discussed in Section V, the RF results are discussed in Section VI and a conclusion is drawn in Section VII.

II. TRANSPARENT UNIT CELL DESIGN

A. *Transparent Conductive Metal Mesh*

As discussed in the previous section, one of the promising solutions to realize an optically transparent conductive surface is metallic mesh in which a portion of a metallic sheet is etched allowing the optical wave to pass through but at the same time preserving a small portion of metal that allows flowing the electromagnetic current. The metal mesh structure that is used in this study is demonstrated in Fig. 1. The pitch (*p*) and width (*w*) of the metal strips determine the transparency of the structure and it can be calculated by [13]:

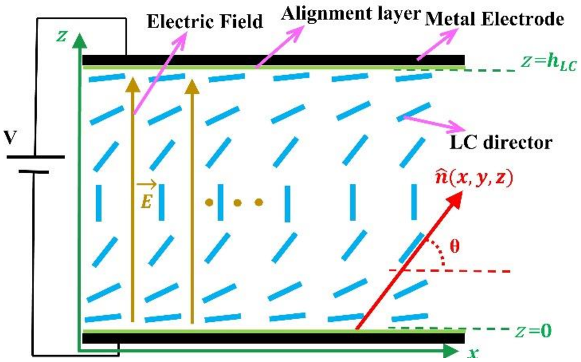

Fig. 2. A general configuration in an LC layer for antenna applications.

$$\psi=\frac{\mathrm{w}}{\mathrm{w+g}} \tag{1}$$

$$T_{mesh}=(1-\psi)^2 \tag{2}$$

$$\mathrm{T_{tot}=T_{mesh}\times T_{sub}} \tag{3}$$

Where ψ is called the filling factor and T_{mesh}, T_{sub} and T_{tot} are the transparency of metal mesh, substrate, and total transparency of the substrate carrying the mesh, respectively. The sheet resistance is:

$$\mathrm{R_s}=\frac{1}{\sigma t(2\psi-\psi^2)} \tag{4}$$

where σ is conductivity and t is the thickness of the metal.

In the current study, copper ($\sigma=5.8\times10^7$) is selected as the metal for the final fabrication with the pitch (*p*) and width (*w*) of 150 µm and 10 µm, respectively. Since the RF frequency is 28 GHz, the metal thickness is considered to be 1.2 µm which is three times higher than the skin depth of copper (0.39 µm) at this frequency. The corresponding transparency and electrical resistance for these values are T_{mesh}= 87.1% and $\mathrm{R_s}$= 0.11 Ω/sq.

An alternative approach for transparency could be using ITO, however, the typical resistivity for ITO is 4-8 Ω/sq [2] which is much higher than metal mesh and consequently results in a much higher loss than metal mesh unitcell, hence, it will not be used in this study.

B. *Liquid Crystal modeling*

From an electromagnetic point of view, LC is an anisotropic material that shows different primitivities in x, y, and z directions, and these primitivities can be changed by applying an external electric or magnetic field. A typical LC cell is displayed in Fig. 2 where the LC material is confined between two metal electrodes with each electrode connected to one terminal of a voltage source. The LC material usually consists of rod-shaped molecules. Among different mesophases of LC, rod-shaped molecules in the nematic phase have an average orientational order. The local average directions of rod-shape molecules are called directors (n) and they are represented by blue rods in Fig. 2. In the chosen coordinate system, which is illustrated in Fig. 2, these directors can be defined as a unit

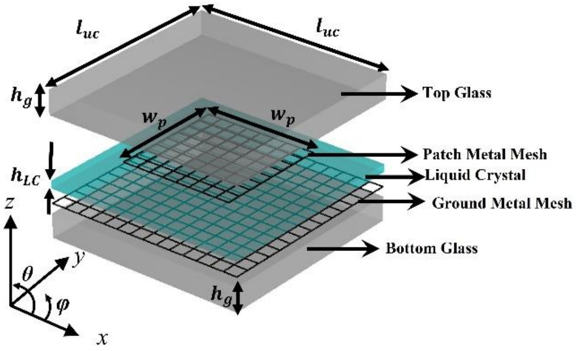

Fig. 3. Configuration of LC-based transparent unit cell. h_g=500 µm, h_{LC}=160 µm, w_p=2400 µm, l_{uc}=4200 µm.

vector in three dimensions [14]:

$$\hat{n} = (n_x, n_y, n_z) \tag{4}$$

$$|n| = \sqrt{n_x^2 + n_y^2 + n_z^2} = 1 \tag{5}$$

In this demonstration, the angle between the director $\hat{n}$ and $\hat{z}$ direction is called tilt angle θ. The permittivity tensor at any infinitesimal volume in the LC space can be obtained by:

$$\bar{\bar{\varepsilon}}_r = \varepsilon_{r\perp} I + \Delta\varepsilon_r \ \hat{n} \otimes \hat{n} \tag{6}$$

Where I is the 3×3 identity matrix, $\Delta\varepsilon_r = \varepsilon_{r||} - \varepsilon_{r\perp}$ is dielectric anisotropy and ⊗ is the tensor product. Moreover, $\varepsilon_{r||}$ and $\varepsilon_{r\perp}$ are permittivity values, parallel and perpendicular to the director, respectively. The same equation can be obtained for loss tangent values in which $\tan\delta_{||}$ and $\tan\delta_{\perp}$ are tangent loss values, parallel and perpendicular to the director, respectively.

If a thin layer of a plastic such as polyimide (PI) (with usually 100-200 nm thickness) is applied on the electrode surface and rubbed with a soft brush in the *x* direction, the microgrooves that are created on the surface can force the LC directors to align in x direction when there is no voltage applied on the electrodes. Usually, the directors are not perfectly aligned in x which can be represented with a pretilt angle. In this study, the pretilt is assumed to be θ = 3°. For the unbiased state, the orientation of LC directors in the entire LC volume is the same as those close to the surface of the alignment layer due to a strong anchoring force. Once the voltage starts to increase, the directors start to align in parallel to the electric field $\vec{E}$. The interaction of electric torque on the LC due to the electrostatic field and elastic force between molecules determines the LC director distribution. The final orientation of directors is obtained by minimizing the free energy functional (Gibbs free energy) which consists of electrostatic, elastic bulk, and surface anchoring force contribution [15]:

$$F = f_D - f_E + f_S \tag{7}$$

Where, f_D is the elastic distortion energy density, f_E is electrostatic energy density and f_s is the free energy density due to the anchoring force on the alignment layers. In (6):

$$f_D = \frac{1}{2} K_{11} (\nabla . \hat{n})^2 + \frac{1}{2} K_{22} \left(\hat{n} . \nabla \times \hat{n} + q_0 \right)^2 + \frac{1}{2} K_{33} |\hat{n} \times \nabla \times \hat{n}|^2 \tag{8}$$

Where, K_{11}, K_{22} and K_{33} are splay, twist, and bend elastic constants. When chiral dopant is added, q_0 determines the chiral state of the system which is zero in this study. Electrostatic energy density can be described as:

$$f_E = \frac{1}{2} \varepsilon_0 \left(\vec{E}_b . \, \overrightarrow{\bar{\bar{\varepsilon}}_r^b . E_b} \right) \tag{9}$$

In (8), $\bar{\bar{\varepsilon}}_r^b$ is the relative permittivity tensor at bias frequency, which itself depends on $\hat{n}$, and $\vec{E}_b$ is an electric field at the bias voltage frequency.

Obtaining the LC director distribution is done by minimizing the LC free energy to update the LC director profile and solving the Gauss law to update the potential profile in an iterative process until the convergence is obtained [16]. This iterative process can be done by the finite difference method. In conventional LC cells like the one illustrated in Fig. 2, where the electric field under the electrodes (unit cell metal) is uniform in the z-direction, the distribution of LC directors can be found by solving a differential equation with the proper boundary condition [17]. Based on the assumption of a uniform electric field in the z-direction for conventional LC cells, LC modeling in commercial electromagnetic software can be done by simply changing the permittivity of the LC block from $\varepsilon_{r\perp}$ to $\varepsilon_{r||}$. For more accurate modeling, one can model the LC as a inhomogeneous anisotropic material in *z* direction by stratifying the LC volume [18]. However, if the surface of the metal electrode contains many defects with arbitrary shapes, finding a differential equation that predicts the director's alignment is almost impossible. Therefore, a finite difference method with a 3D modeling capability is required. In this study, modeling the LC director distribution has been done by using Shintech Optics LCD Master 3D simulation software. This software is capable of accurately obtaining both director distribution and optical behavior of an LC cell with a wide variety of options. In this study, we will only use the LC director solver.

C. *Reconfigurable Transparent RA Unit cell*

Since LC materials are transparent, one can use the features of LC combined with the transparent nature of metal mesh to realize a transparent reconfigurable unit cell. The conventional LC-based RA can consist of tens of simple unit cells such as those proposed in [19], [20], and [21]. However, in the conventional modeling of LC cells, the electrostatic bias field can be considered uniform in the *x*, *y*, and *z* directions. Moreover, the fringing fields in LC volume at the edge of the radiating element could affect reflection magnitude and phase. This phenomenon can be also modeled by stratifying the LC [22]. Nevertheless, using the Fouquet port simulation to obtain phase shift and loss, does not normally require any LC director modeling due to insignificant errors. As a result, the electromagnetic analysis of the unit cell can be carried out

TABLE I
GT7-29001 PARAMETERS USED IN THE DIRECTOR SIMULATION

Para.	Value	Para.	Value	Para.	Value
K_{11}	14.3 (pN)	$\varepsilon^{b}_{r\perp}$	4.6	$\varepsilon^{b}_{r\|\|}$	26.7
K_{22}	$\approx 0.5*K_{11}$	$\varepsilon^{rf}_{r\perp}$	2.45	$\varepsilon^{rf}_{r\|\|}$	3.53
K_{33}	18.7 (pN)	$tan\delta^{rf}_{\perp}$	0.0117	$tan\delta^{rf}_{\|\|}$	0.0064
γ_{rot}	0.316 (Pa.s)	V_0	0.85 V		

directly in full-wave Electromagnetic (EM) software such as CST Microwave Studio if the values of $\varepsilon_{r\perp}$ and $\varepsilon_{r||}$ are known at the RF operating frequency. If the metal part of the unit cell do not have relatively large defects, an accurate modeling can be done following the method proposed in [22] by incorporating the anisotropic nature of LC and inhomogeneity around the edge where fringing fields exit. Fig. 3 depicts a metal mesh-based unit cell where the liquid crystal is injected between two copper-coated glass substrates. The bias line is not considered in the unitcell simulation to make the director modeling easier. The width bias line is 15 µm therefore the resistance is high, and it can be connected to the patch wherein the electric field has a null. With this arrangement the effect of bias line is insignificant and can be ignored. Nevertheless, it is considered in RA full wave simulation which also shows insignificant impact. Since the metal mesh has defects all over the metallization, the electric field is highly inhomogeneous in the *x*, *y*, and *z* directions. Consequently, the anisotropic permittivity tensor is inhomogeneous in the *x*, *y*, and *z* directions. Therefore, accurate modeling of director distribution is required to model the EM response. The design procedure of the proposed reconfigurable transparent unit cell can be demonstrated in several steps, as it is shown in Fig. 4. In the first step, based on the transparency requirement, frequency, and fabrication limitations, one can choose the proper dimensions for mesh width (*w*), pitch (*p*), metal thickness (t) along with unit cell dimensions such as patch size, unit cell size, LC height.

Given that metal patterning on a glass substrate requires photolithography followed by the etching or lift-off process, the width of the metal line (*w*) with respect to metal thickness (*t*) should be selected so that the etching or lift-off process yields the best results without defects such as under etching, etc. The choice of pitch size should be small enough to avoid wave leakage from the ground plane. This issue is further discussed in the next section. However, a small pitch (*p*) requires a smaller mesh width (*w*) to keep the same transparency. On the other hand, making a small line width (*w*) is difficult with a high metal thickness. Therefore, choosing the mesh parameters is a compromise. To make the numerical simulation shorter, metal mesh parameters in this section are selected to be *p*=300 µm and *w* = 20 µm. However, it gives the same surface resistivity and transparency as Section II.A. T24003 fused silica wafer with a permittivity of 3.8 and tangent loss of 0.002 is used for the substrate. The measured optical transparency of the glass is 94.5%. Hence, the total transparency of the unit cell can be calculated as:

$$\mathrm{T_{uc}=T_{mesh}\times T_{sub}\times T_{mesh}\times T_{sub}=67.7\ \%}$$

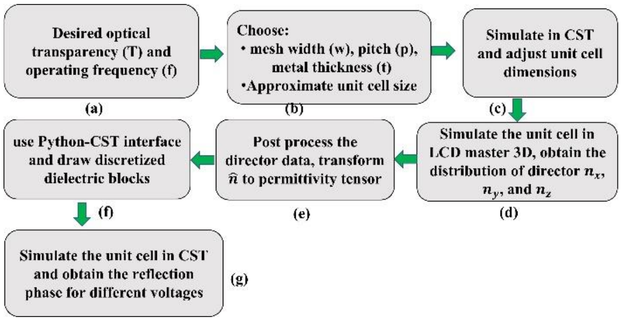

Fig. 4. Design steps for transparent unit cell based on LC material.

Since the liquid crystal and polyimide are very thin, their contribution to the theoretical calculation is ignored for now but it will be discussed in the measurement section. It should be noted that the calculated transparency is the worst-case scenario where it is assumed that the top glass is entirely covered with metal mesh and the two mesh layers are misaligned. However, we can see that the top glass is only covered with the patch area and if the mesh layers are perfectly aligned, the total transparency can be increased.

The liquid crystal used in this work is GT7-29001 from Merck Electronics KGaA, Darmstadt, Germany. The specification of the material that is needed to model the LC throughout this paper is summarized in Table I. Once the physical dimensions of the unit cell are chosen, we can simulate the unbiased unit cell and obtain the reflection loss and phase (step (c) in Fig. 4). The electromagnetic simulations of the unit cell in this study have been done in CST Microwave Studio with unit cell boundary condition. For evaluating the metal mesh parameters on unit cell response, LC is assumed to be unbiased for which all the directors are parallel to the *x*-direction ($\theta = 0$), and the (6) simplifies to a diagonal tensor:

$$\bar{\bar{\varepsilon}}_{\mathrm{V=0}} = \begin{pmatrix} \varepsilon_{\mathrm{r}||} & 0 & 0 \\ 0 & \varepsilon_{\mathrm{r}\perp} & 0 \\ 0 & 0 & \varepsilon_{\mathrm{r}\perp} \end{pmatrix} \tag{10}$$

$$\overline{\overline{\tan\delta}}_{\mathrm{V=0}} = \begin{pmatrix} \tan\delta_{||} & 0 & 0 \\ 0 & \tan\delta_{\perp} & 0 \\ 0 & 0 & \tan\delta_{\perp} \end{pmatrix} \tag{11}$$

If the applied voltage is much higher than the threshold voltage, then (6) simplifies to (12), only for the locations where the directors are perfectly aligning in the z-direction:

$$\bar{\bar{\varepsilon}}_{\mathrm{V\gg0}} = \begin{pmatrix} \varepsilon_{\mathrm{r}\perp} & 0 & 0 \\ 0 & \varepsilon_{\mathrm{r}\perp} & 0 \\ 0 & 0 & \varepsilon_{\mathrm{r}||} \end{pmatrix} \tag{12}$$

$$\overline{\overline{\tan\delta}}_{\mathrm{V\gg0}} = \begin{pmatrix} \tan\delta_{\perp} & 0 & 0 \\ 0 & \tan\delta_{\perp} & 0 \\ 0 & 0 & \tan\delta_{||} \end{pmatrix} \tag{13}$$

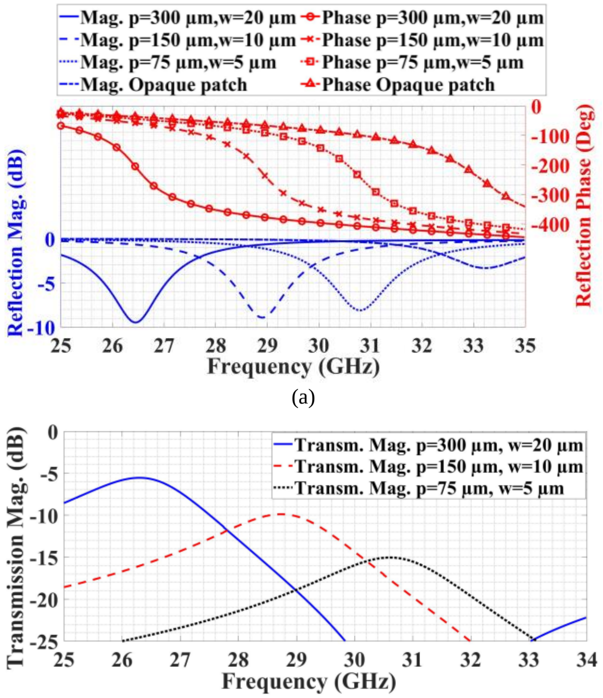

(a)

(b)

Fig. 5. Mesh parameters effect (p and w) on (a) reflection and (b) transmission coefficients of the unit cell.

Equations (10) and (11) are used throughout this work to model the entire LC volume for the unbiased state. Fig. 5(a) compares the reflection coefficient of several metal mesh settings and opaque unit cells, illuminated with an x-polarized plane wave in a periodic boundary condition. The defects in metal mesh, not only increase the loss due to higher resistance but also, the inductance of the narrow metal lines decreases the resonant frequency of the unit cell with equal size. Therefore, the size of the unit cell (l_{uc} and w_p) needs to be optimized based on the desired surface resistance (or transparency) of the metal mesh. Another issue worth mentioning is the transmission coefficient. The effect of pitch (p) and width (w) on reflection and transmission coefficient can be seen in Fig. 5(b). Even by keeping the surface resistance constant, increasing the pitch size would increase the transmission coefficient. Therefore, achieving high transparency in the reflective unit cell requires a small pitch size and small width. It should be noted that in a conventional LC-based unit cell, besides the tangent loss, LC thickness h_{LC} usually determines the reflection loss and normally, increasing the LC thickness reduces the reflection loss and phase shift. After adjusting the physical dimensions, we need to obtain the director distribution in the presence of a biased electric field to evaluate the phase-shifting performance. To do so, the unit cell is simulated in Shintech Optics LCD Master 3D simulation software and using the values presented in Table I. Since the software solves the equation of section II.B in a finite space, the boundary condition in the *z*-direction is Neuman and in the *x*-*y* direction is set to be periodic. Moreover, it is an electrostatic simulation, and changing the patch and ground size does not have a significant effect on the simulation results. Therefore, a smaller unit cell in case of patch and ground size is simulated to reduce the simulation time and resources. The LC thickness, pitch size (p), and width (w) of the metal mesh are kept the same. The simulated unit cell's physical dimensions are listed in TABLE II. It is worth mentioning that the polyimide layer thickness is set to 200 nm. Fig. 6 shows the angle of directors (θ) along with black rods which is a representative of LC directors itself, in the *x*-*z* plane cross-section for different voltages. To better demonstrate the distribution of directors, the figures are zoomed to half of the entire unit cell cross-section. Director distribution in 0 V is not shown here since all the directors are aligned in the *x* direction. The cross-section of metal mesh lines is also illustrated with brown rectangular blocks. Since the threshold voltage (V_{th}) for GT7 is around 0.85 V, after this voltage, the electric torque exceeds the elastic one and the directors start to align more and more with the increase of the electric bias field. Up to 6 V, only the director below the metal mesh is rotated 90º. However, after this voltage, the directors between the two metal lines also started to rotate. As we increase the voltage, the interaction of elastic forces and the electric fields will create a peak between metal lines. This phenomenon could stem from the interaction of adjacent metal lines on top and bottom electrodes in the diagonal direction. After 30 V, there is no significant change in the director distribution. It can be seen that the directors are almost perpendicular to the alignment layers in the volume between z = 50 µm to z = 110 µm.

TABLE II
UNIT CELL DIMENSIONS USED IN LCD MASTER 3D SIMULATION SOFTWARE

Para.	Value (µm)	Para.	Value (µm)
p	300	W_p	2120
w	20	l_{uc}	3320
h_{LC}	160 µm	h_g	500

Since the LC alignment is not uniform, the effective permittivity range is unknown, and the phase shift of the unit cell cannot be calculated accurately without considering the non-uniform director distribution. To gain insight into the 3D distribution of the directors in the entire surface of the unit cell, Fig. 7 shows the director distribution in a quarter of the unit cell, in the *x*-*y* plane cross-section near the top electrode at z = 136 µm. Due to the periodic nature of the metal mesh structure, we can observe a regular pattern of alignment in different regions within a unit cell. By observing this plot and the edge of the metal patch in Fig 6, we can divide the whole unit cell into different regions and assume that the director distribution is the same for all the mesh pitches across each region. Fig. 8 denotes the regions in a quarter of the unit cell. The director distribution has a symmetry along the *x* and *y* axis around the center of the unit cell in the entire volume of LC. For each region, we can assume that the director distribution of all the pitches is the same. Therefore, we can model the unit cell by using the data of one pitch in each region and then copy that data to the whole region. At the next step, the

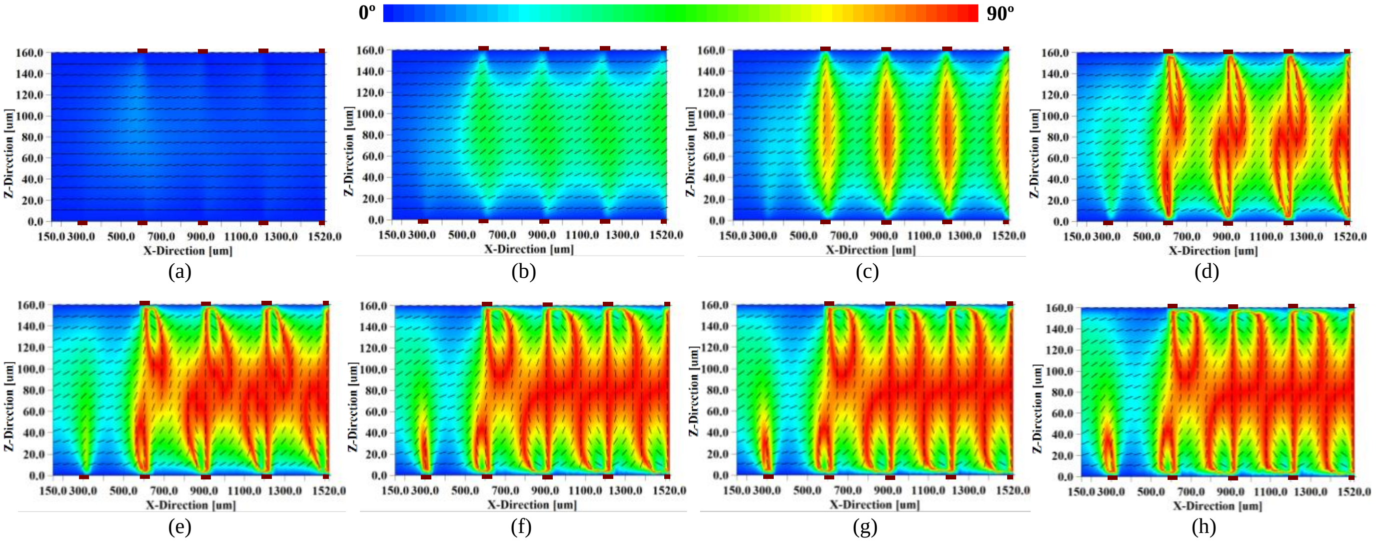

(a) (b) (c) (d)

(e) (f) (g) (h)

Fig. 6. Angle of directors (θ) and director representation (black rods) of LC in the plane of y =1360 μm (between two metal strips), for (a) 1 V, (b) 2 V, (c) 3 V, (d) 6 V, (e) 12 V, (f) 30 V, (g) 40 V, and (h) 60 V.

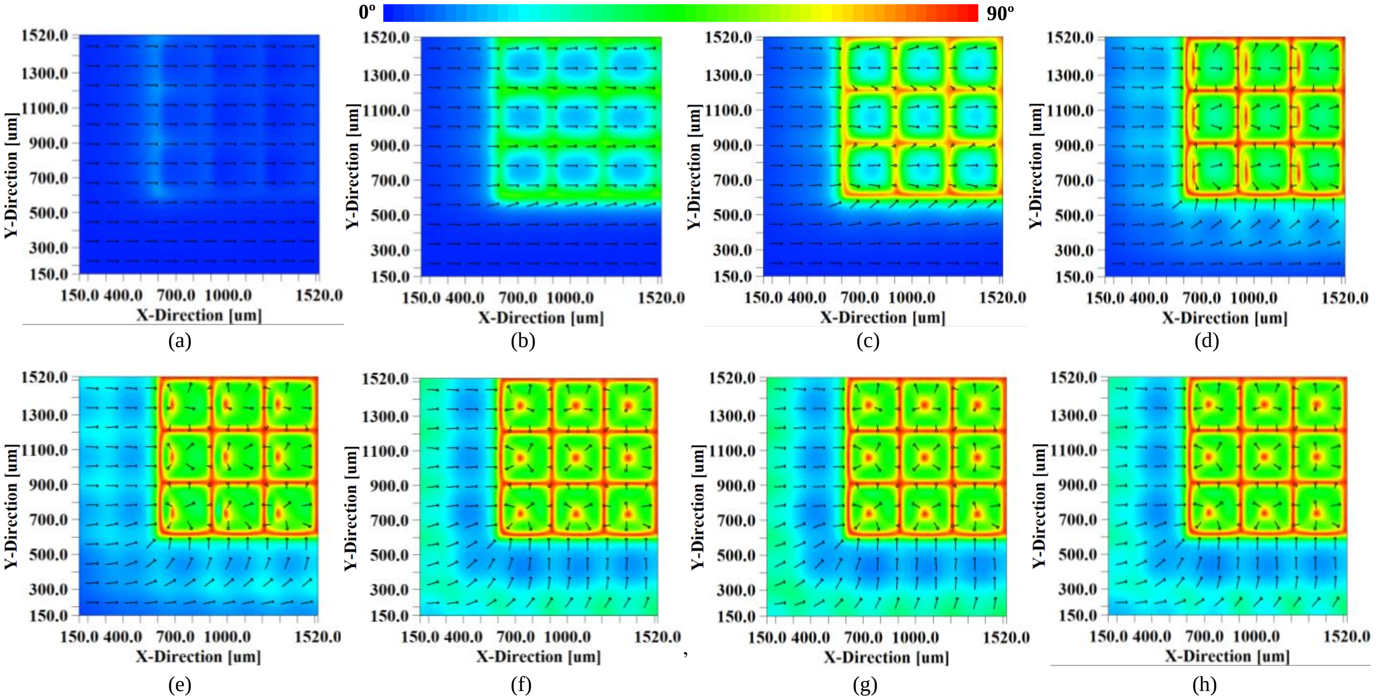

(a) (b) (c) (d)

(e) (f) (g) (h)

Fig. 7. Angle of directors (θ) and director representation (black rods) of LC in the plane of z =136 μm (near the metal), for (a) 1 V, (b) 2 V, (c) 3 V, (d) 6 V, (e) 12 V, (f) 30 V, (g) 40 V, and (h) 60 V.

director unit vectors are exported for the entire LC volume in 1 μm step width. Then, by using (6) and the values of RF permittivity in Table I, the permittivity tensors can be calculated in the entire cell (step (e) in Fig. 4). The same procedure can be performed to obtain the tanδ tensors. In each pitch of the metal mesh, the permittivity tensor is highly anisotropic and inhomogeneous. In the material definition of CST microwave studio, only the diagonal tensors of two extreme cases of fully biased and unbiased can be modeled by using the tensors presented in (10)-(13). However, here we have a non-diagonal tensor, and we will model the LC via the Macros "Create Full Tensor Material'' in CST. In this "Macros", each element of the 3×3 matrix consists of the real and imaginary part of the permittivity so we can model the anisotropic LC material accurately in each point. To model the inhomogeneity, we will discretize the volume in one pitch of the metal mesh per region and then copy that to the whole volume of the corresponding region. Then the structure is simulated in the unit cell boundary condition in CST with Floquet ports on top and bottom of the unit cell. The discretization is done by dividing the volume into several blocks in the x, y, and z directions. For each block, we would

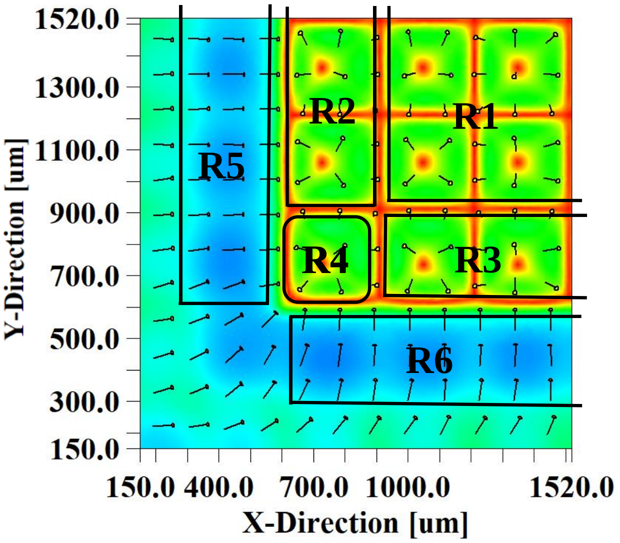

Fig. 8. Outlining different regions in a quarter of the entire unit cell in which the directors are repeating the same pattern in mesh pitches.

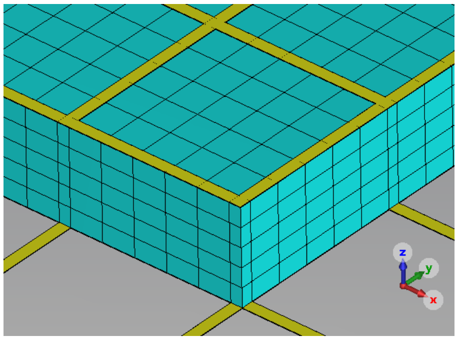

Fig. 9. A discretization example with Nxy = 5 and Nz = 5 for LC blocks between metal strips.

TABLE III

DISCRETIZATION PARAMETERS IN BETWEEN METAL AREAS FOR ONE PITCH

Nxy / Nz	2	5	10	14
2	🟩	🟩	🟩	
5	🟩	🟩	🟩	
10	🟩	🟩	🟩	
16				🟩

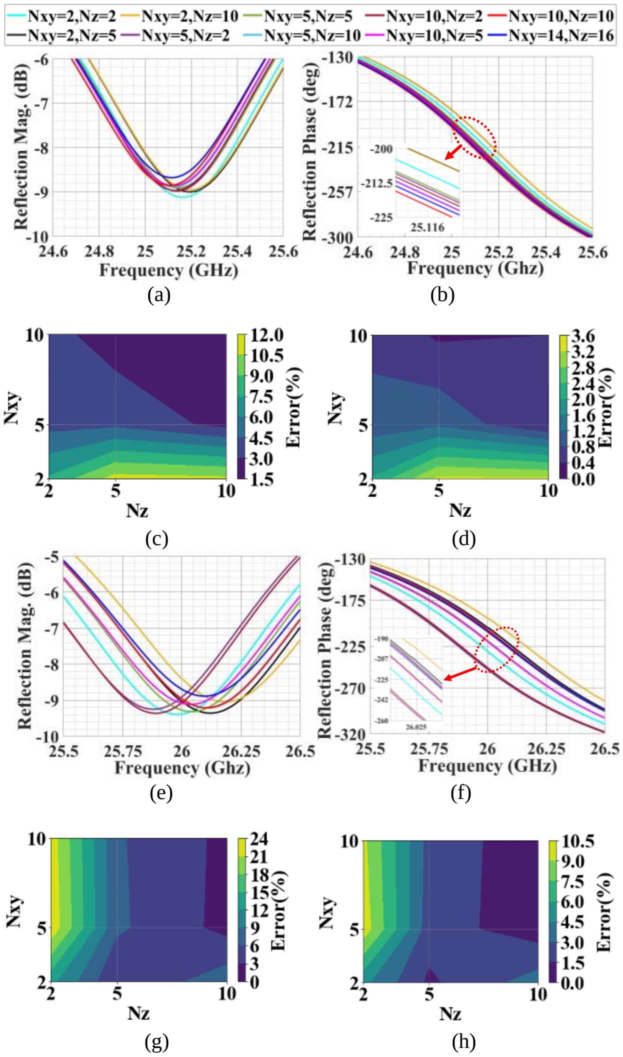

(a) (b)

(c) (d)

(e) (f)

(g) (h)

Fig. 10. Reflection (a) magnitude and (b) phase over frequency for different discretization steps of V_{bias} = 40 V. Reflection (c) magnitude and (d) phase error percentage for different discretization parameters of V_{bias} = 40 V. Reflection (e) magnitude and (f) phase over frequency for different discretization steps of V_{bias} = 2 V. Reflection (g) magnitude and (d) phase error percentage for different discretization parameters of V_{bias} = 2 V.

assign the permittivity tensor of the center point to the whole block. An example of discretization with Nxy = 5 and Nz = 5 steps in between metals is demonstrated in Fig. 9. It should be noted that the smallest dimension of those blocks that are below the metal area is the same as the width (*w*) of the metal mesh. To reduce the computation cost, we only considered regions R1-R4. R5 and R6 are not considered in the RF calculations since the LC alignment is very weak and one can assume that the LC is unbiased. For RF simulations, we will apply the obtained director distribution to a unit cell with the patch and ground size of 2400 µm and 4200 µm respectively, with an operating frequency near 26 GHz. The rest of the parameters are the same as TABLE II. It consists of 64 metal mesh steps ($(2400/300)^2$). In the next step (step (f) in Fig. 4), a code is developed in Python that takes the permittivity tensor data with the resolution of 1 µm in *x*, *y*, and *z*, and then uses the CST Python Libraries to draw the blocks in the LC volume for different discretization. All the combinations of discretization steps in the x-y plane and z-direction that are used in one pitch of the metal mesh are demonstrated in TABLE III. The setting of "Nxy =14" and "Nz =16" is selected as the reference for error calculation. The unit cell is simulated for 40 V, and 2 V as an example with the discretization setting of TABLE III, and errors are calculated for each one, respectively. The calculated error of different discretization steps for reflection magnitude and phase of two voltages is demonstrated in Fig. 10. It can be observed that as the discretization step is reduced, the phase error is decreased. The maximum phase error around the resonant frequency for 40 V and 2 V biasing voltage is 15.5° and 40°. In general, the error is higher for 2 V since for the 40 V state, in the regions where the RF field intensity is higher, the LC is fully biased

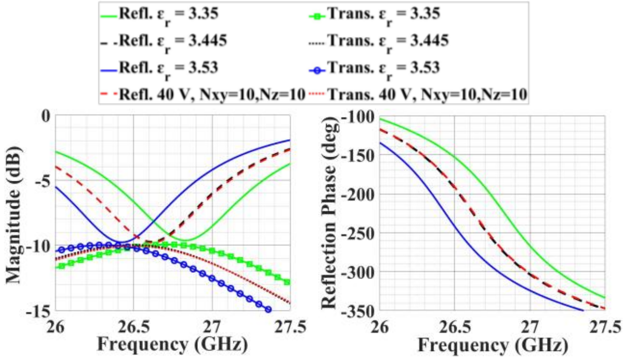

(a) (b)

Fig. 11. Isotropic approximation of fully biased unit cell reflection coefficient with different values of permittivity compared with accurate (anisotropic and inhomogeneous) discretized result for (a) magnitude (reflection and transmission) and (b) reflection phase.

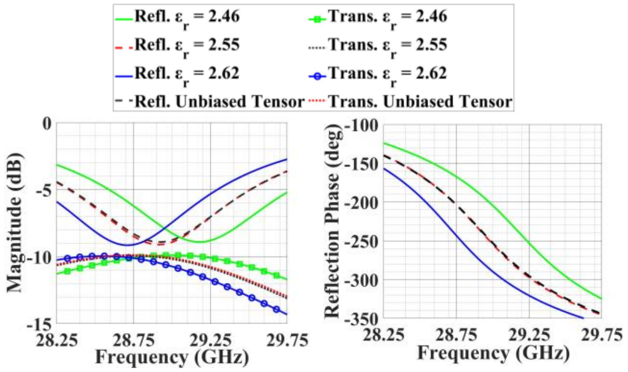

(a) (b)

Fig. 12. Isotropic approximation of unbiased unit cell reflection coefficient with different values of permittivity compared with accurate anisotropic tensor results for (a) magnitude and (b) phase.

thus the different discretization step has less RF response deviation. Most of the simulation time is due to the frequency domain tetrahedral mesh generation process and the actual solver simulation time is negligible when the initial mesh is generated. Fig. 5(a) (unbiased) and Fig. 10(b) (fully biased) show that the unit cell, based on transparent metallic mesh with LC substrate can provide more than 180° phase shift which is enough for beam-steering application.

III. REFLECTARRAY DESIGN

In the previous sections, we demonstrated that the mesh structure can provide enough phase shift when it is combined with LC material despite the highly inhomogeneous and anisotropic bias field. It should be repeated that for investigating the LC performance in the presence of metal mesh, we choose p = 300 μm and w = 20 μm to reduce the simulation time by reducing the number of dielectric blocks in the entire unit cell. However, for the RA realization, the better choice for metal mesh parameters is the smallest pitch (p) and width (*w*) that is achievable for the desired transparency since, a) we need to minimize transmission leakage, and b) we need the most uniform electrostatic field below patch to improve realized anisotropy of LC. However, achieving a relatively small pitch and width size in the photolithography process is not easy, especially with a thick metal layer. To make a compromise between small metal features and fabrication quality, we chose p = 150 μm, and w =10 μm for the final RA fabrication.

A. Final Unit Cell design

In the first step, a unit cell is designed in CST and LCD Master 3D simulation software with the following parameters: p = 150 μm, w = 10 μm, h_g= 500 μm, h_{LC} = 160 μm, w_p = 2400 μm, l_{uc}= 4200 μm. Once the simulation is done in LCD master 3D and the director data distribution is obtained, CST Microwave Studio is used to evaluate the phase shifting performance. The unit cell is discretized with Nxy =10 and Nz =10 (which is a compromise between simulation time and accuracy) and it was simulated with unit cell boundary condition for the 40V case which gives the maximum phase shift. Since the RA consists of many unit cells and any voltage between 0V to 40 V can be assigned to them for the beam steering, we need to simulate all these states in LCD master and CST Microwave Studio to obtain a phase curve that covers all the voltage states. This is a very time-consuming approach. Instead, we can consider the 40V state as the maximum achievable phase shift and model the active LC volume with single block LC in CST simulation. It can be noted here that once the unit cell with certain physical parameters and a certain LC type is simulated, then the approximate maximum voltage, required for the full bias can be obtained, and unnecessary high-voltage hardware implementation can be avoided. Next, the permittivity of this LC block is swept to match the accurate results obtained from the discretization method. The simulation results of this approach are demonstrated in Fig. 11. It shows that for $\varepsilon_r =$ 3.445, the reflection loss and phase shift are very close to the discretized model.

To obtain the phase shift, an unbiased state needs to be simulated as well. In Section II.C (Fig. 5), the unbiased state for p = 150 μm, w = 10 μm has been simulated in which the LC was modeled by an anisotropic tensor presented in (10) and (11). Since the metal mesh introduces anisotropic and inhomogeneous bias fields in the LC volume, the isotropic modeling of LC material will lead to a large reflection response error if we assume that the isotropic permittivity is $\varepsilon_{r\perp}$= 2.45. The same procedure as 40 V (fully biased state) needs to be repeated to obtain the unbiased permittivity value of a single block LC that can be used to approximate the anisotropic LC tensor. The reflection loss and phase shift for unbiased LC modeling are presented in Fig. 12 which shows that ε_r= 2.55 can be used in the entire LC volume to approximate the anisotropic behavior of LC. Based on the presented results, a single block of isotropic normal material definition with a permittivity range of $\varepsilon_{r\perp}$=2.55 to $\varepsilon_{r\|}$=3.445 can model the GT7 LC behavior. The simulated reflection coefficient shows around 9.5 dB loss and 253° phase shift.

B. RA Simulation Results

Since the RA is extremely large compared to the width (*w*) of metal mesh, the number of mesh cells is significant. Time

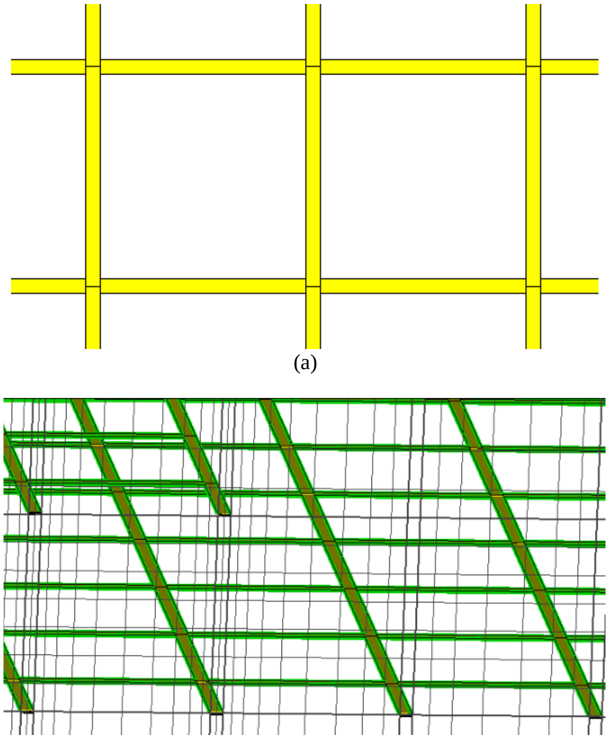

(a)

(b)

Fig. 13. Demonstration of time domain meshing strategy for transparent RA. (a) separate building blocks of the metal constituting the total RA and (b) local hexahedral mesh lines concentrated more around the metallization.

Domain Solver in CST is used to simulate the RA to obtain the far-field radiation pattern. A technique has been used to ensure that results are accurate with the least mesh cells. The metal mesh lines of each pitch are divided into separate blocks instead of merging all the blocks. Then a local Mesh Group is assigned to these metal blocks in a way that ensures having at least 2 mesh lines across the width of the metal blocks. These separate blocks that constitute the RA are illustrated in Fig. 13(a). Since the RF electric field is concentrated near the metal parts, by activating the "Smooth Mesh with Equilibrate Ratio" option in CST Microwave Studio, we will adopt an accurate meshing strategy. The time domain Hexahedral mesh lines are demonstrated in Fig. 13(b). Finally, a 10×10 element RA with an offset feed is simulated where a coaxial probe-fed horn with a model of "PASTERNACK PE9851/2F-10" operating from 22 GHz to 33 GHz with 10 dB nominal gain is used to illuminate the RA. As an example, the simulated 3D radiation pattern for beam direction of φ = 0 and θ = -20˚ is illustrated in Fig. 14. The simulated 2D radiation pattern for different beam directions is presented in Fig. 15 that demonstrates the 3-dB beam steering from -15˚ to + 55˚ in the E-plane and from -55˚ to +55˚ in the H-plane. The peak gain occurs at 28.5 GHz with a maximum of 16 dBi for θ = +20˚ in the E-plane.

IV. TRANSPARENT RA FABRICATION

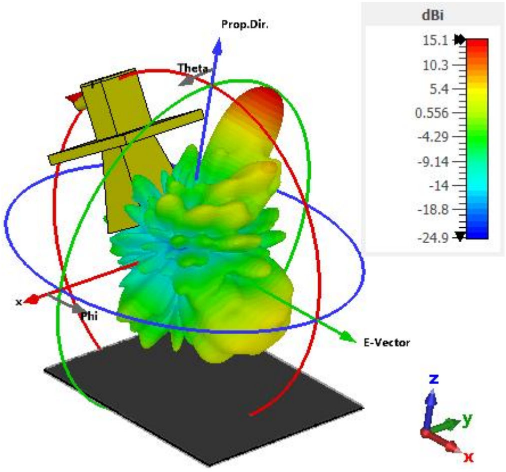

Fig. 14. Simulated 3D radiation pattern for beam directions of φ = +90, θ = +20˚ at 28.5 GHz.

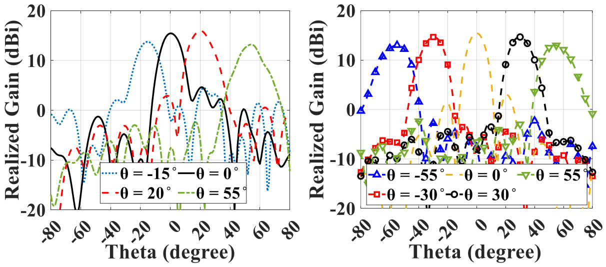

(a) (b)

Fig. 15. Simulated beam-steering radiation pattern for (a) φ = 90˚ and (b) φ = 0˚ plane.

The fabrication of a transparent LC-based antenna starts with the photolithography process of the clean fused silica substrate to create the antenna metal pattern on it. Two substrates are used, one for patch elements and the other one for the ground plane. The lift-off process is used to create the metal pattern on the glasses. It is started by coating the substrates with photoresist and then exposing them with the corresponding mask. Next, the photoresist is removed and then the metal deposition is done by Physical Vapor Deposition (PVD) method for Chromium, Copper, and Gold with 10 nm, 1.2 µm, and 20 nm thickness, respectively. Then the excessive photoresist is removed with the Lift-off process and the final pattern will emerge. The fabricated ground and patch substrates are shown in Fig. 16(a) and (b), respectively. It should be noted that the measured optical transparency of the clean Fused Silica substrate is 94.5%. The optical transmission measurement of the patch substrate and ground substrate shows an optical transparency of approximately 84 % and 83%, respectively, which agrees well with the theoretical calculations of Section II. In the next step, the polyimide which acts as the pre-alignment layer is coated on both substrates with 200-300 nm thickness, then the substrates are baked in the oven and rubbed with velvet cloth in the x-direction.

Since the final target is to maximize the optical transparency of the fabricated sample, the method to realize the LC cavity thickness needs to be compatible with the

(a) (b)

Fig. 16. Fabricated metal patterns on fused silica glass for (a) patch layer and (b) ground layer.

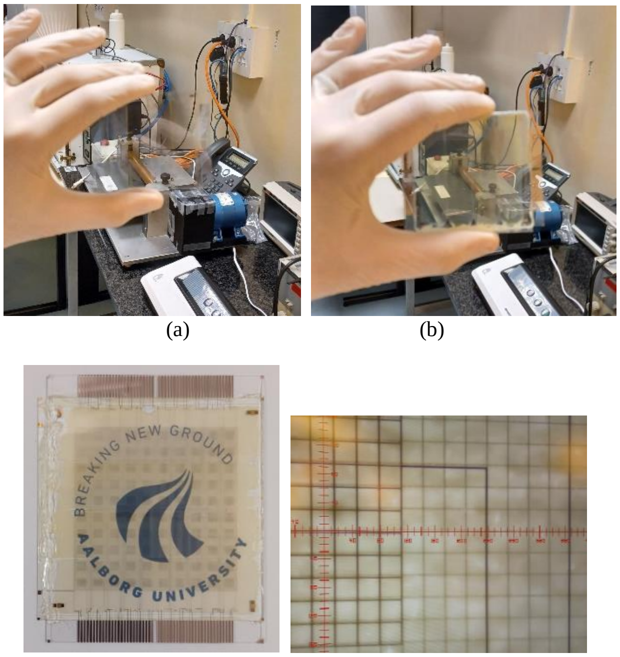

(a) (b)

(c) (d)

Fig. 17. Fully assembled samples with fiber optic spacers. (a) empty assembled sample without LC and (b) RA sample, filled with GT7 LC. (c) the RA sample filled with LC above a text. (d) zoom in view on 2 layers showing the alignment of two metal mesh layers.

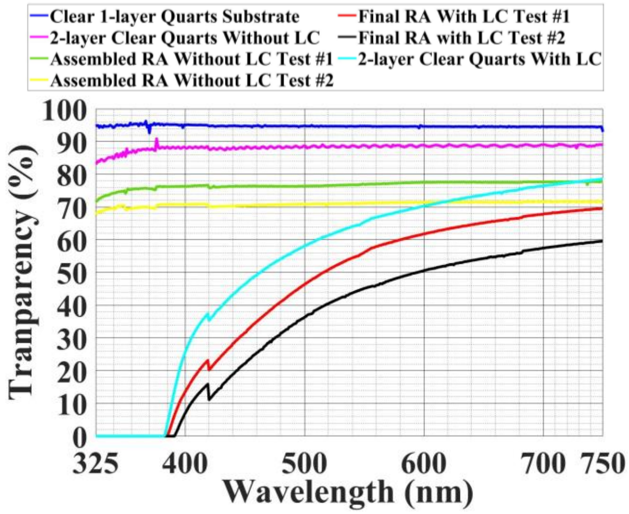

Fig. 18. Measured transparency of fabricated samples in the optical spectrum for empty RA and filled RA with GT7.

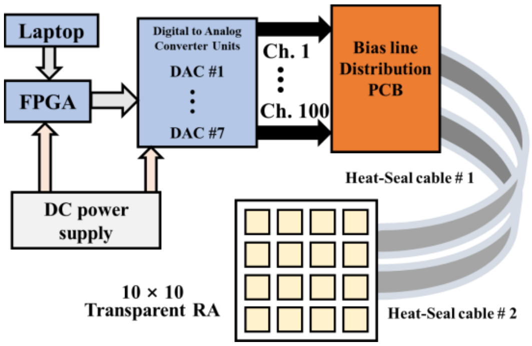

Fig. 19. Block diagram of AC voltage addressing.

optical requirements. One of the best solutions for this goal is to use SU-8 permanent negative epoxy photoresist which has above 95% optical transparency. One other feature that might be relevant here is the dielectric constant which is 3.2 which is close to the LC dielectric constant. The LC cavity in this study is 160 μm. However, due to high thickness and viscosity in addition to the large substrate size, it can not yield a homogeneous thickness across the entire substrate. It should be noted that this method is sufficiently repeatable and yields a smooth thickness below 100 μm.

Since the thickness inhomogeneity can lead to a deteriorated performance, a more reliable solution is to use optical fibers as a spacer for the LC cavity. Although both the core and cladding of fiber are almost transparent, due to the cylindrical shape and different refractive index of the material, they are visible. An optical fiber with a 160 μm cladding diameter is chosen and the LC cavity is realized. Two sides of the RA are sealed with the UV glue and LC material is injected with the capillary force. Then the other two sides are sealed. Fig 17 (a) and (b) show the assembled sample with and without the injected LC in a normal background. Fig. 17(c) shows the sample above a text background. It can be seen that the color of RA that is filled with GT7 is light milky to yellow. The natural GT7 color is light milky but the exposure to UV during the assembly makes it light yellow which could be minimized during the process by covering the LC part with UV protection layers. Fig. 17(d) presents a zoom-in view of the patch layer on top of the ground plane. It shows that the alignment of the two layers is perfect in the y-direction but there is a 10 μm to 15 μm misalignment in the x-direction because of manual alignment.

V. OPTICAL MEASUREMENT AND DISCUSSION

The transmission spectra of the fabricated prototypes are measured in the optical range and it is shown in Fig. 18. A sample filled with LC and no metal on silica glasses is also measured and presented. The empty device has higher than 70% transparency over the entire optical spectrum. Once it is filled with GT7 LC material, the transparency becomes sensitive to the optical wavelength. However, the transparency is still very good to the naked eye as can be seen from Fig 17(c). Unlike the conventional LCs such as 5CB or E7 which are developed for the LCD industry with high optical

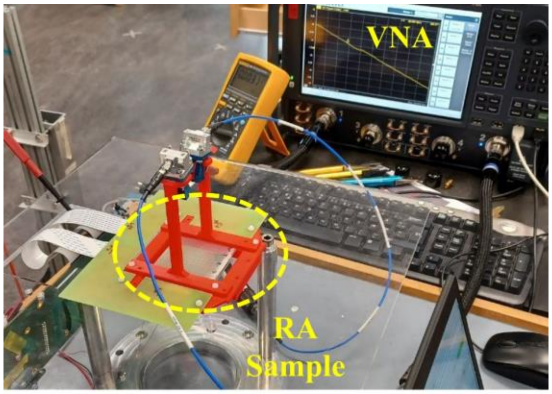

Fig. 20. Reflection phase measurement setup.

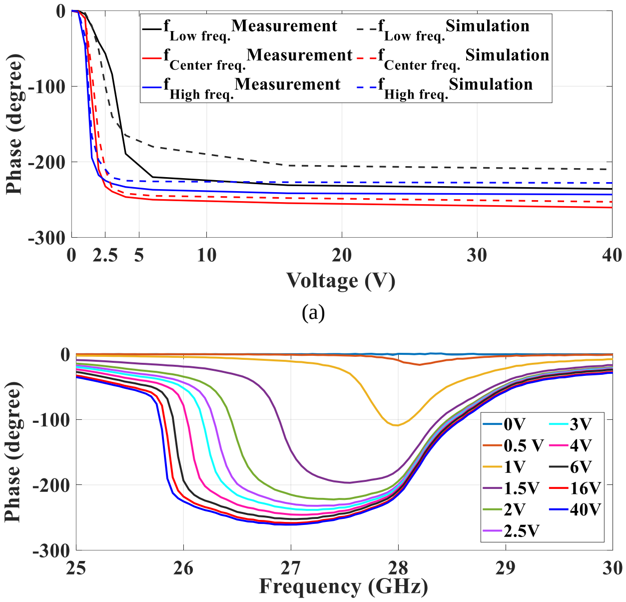

(a)

(b)

Fig. 21. (a) Simulated and measured phase-voltage curve for the transparent RA from 0 V to 40 V for three frequency samples. (b) measured reflection phase curve over frequency.

transparency, the GT7 LC material is specially developed for microwave spectrum applications, thus the optical transparency is not addressed. Another point is that here the LC thickness is high but for lower thickness, the transparency can be improved with GT7. It should be mentioned that GT7 is sensitive to daylight, especially UV, thus it should not be exposed to daylight for a long time. Nevertheless, for the optically transparent RF devices based on LC, at this moment, LC materials such as BL006, 5CB, and E7 can be used which have lower anisotropy (which means lower phase shift) but they have stable and higher optical transparency. Ultimately, new LC mixtures should be developed that have high optical transparency and high microwave anisotropy, simultaneously.

VI. RF MEASUREMENT AND DISCUSSION

A. Bias Circuit Implementation

The block diagram of the control circuit that provides 100 individual variable AC bias voltages for the RA is demonstrated in Fig. 19. A Field Programmable Gate Array (FPGA) is used to control the DAC blocks. It generates defined sequences according to the different beam directions and their corresponding phase distributions. Seven Digital-to-Analog Converters (DACs) of the model DAC81416 from Texas Instrument, each with 16 output channels, transform the digital sequences into 100 analog AC voltages. The DACs provide 1 kHz square wave with 16-bit resolution. The voltages are applied to each patch element through Heat Seal cables. A Heat Seal cable is a kind of flexible cable, in which carbon or silver ink is used as a conductor to be printed on a polyester (PET) film. The cables are directly attached to the voltage pads on the glass with a pressure and heat process. The other side of the heat-seal connector is attached to a PCB.

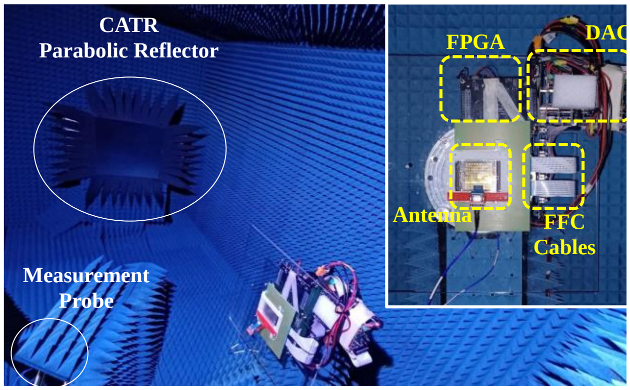

Fig. 22. Radiation pattern measurement setup in the anechoic chamber.

B. Reflection Phase Measurement

A major step in the LC-based antenna design is to obtain the phase-voltage curve with which we will compensate for the phase delay of the wave along the RA that is radiated from the feed horn. A free space measurement can be carried out, with one horn for illuminating the RA surface and the other one for receiving the reflected wave. The measurement setup is shown in Fig. 20. The two horns are located above the RA surface and connected to a Vector Network Analyzer (VNA) and all the unit cells are connected to a common variable AC voltage. The voltage is increased and the phase of S_{12} is measured for different voltage levels. The maximum measured phase shift is around 26.9 GHz. However, the maximum simulated phase shift happens at 27.65 GHz with a 253˚ phase shift. The measured phase-voltage curve is displayed in Fig. 21(a) for three frequencies (center frequency and ±0.75 GHz) which shows 260˚ of measured phase shift from 0 V to 40 V at the center frequency. The results show the same trend for both simulation and measurement. Moreover, the measured normalized reflection phase over frequency for different voltages is demonstrated in Fig. 21(b) which shows that the maximum phase shift occurs around 26.9 GHz. The discrepancy is due to fabrication error and the non-ideal free space measurement of the phase-voltage curve. Since the number of elements is limited, the periodic boundary condition in the free space measurement cannot be fulfilled thus the contribution from edges and non-ideal plane wave illumination can lead to errors. Another possible source of discrepancy is fabrication error. One source of fabrication

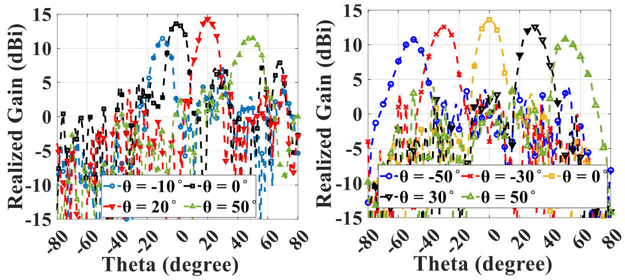

(a) (b)

Fig. 23. Measured beam-steering radiation pattern for (a) φ = 90˚(E-)plane and (b) φ = 0˚(H-)plane at the center frequency (f =27.5 GHz)

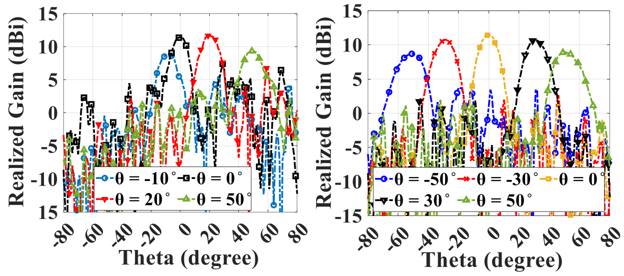

(a) (b)

Fig. 24. Measured beam-steering radiation pattern for (a) φ = 90˚(E-)plane and (b) φ = 0˚(H-)plane at a lower frequency (f =26.75 GHz)

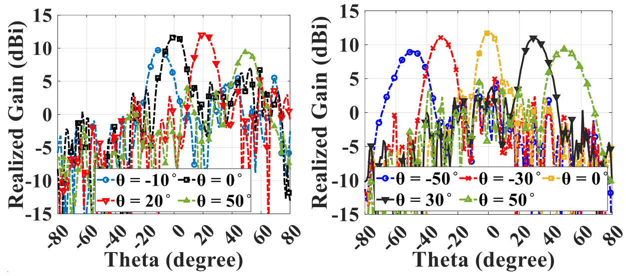

(a) (b)

Fig. 25. Measured beam-steering radiation pattern for (a) φ = 90˚(E-)plane and (b) φ = 0˚(H-)plane at a higher frequency (f =28.25 GHz)

error is the LC pre-alignment distortion around the optical fiber that is used for LC cavity realization. This can cause resonant frequency deviation for different unicells at the unbiased state. The large LC layer thickness can also exacerbate the pre-alignment distortion due to the decrease in anchoring force. Another source of fabrication error is the imperfect assembly of fiber optics and glass substrates.

C. *Radiation Pattern Measurement*

The far-field pattern measurement setup is presented in Fig. 22 where the DACs, FPGA, and antenna sample are shown. The measurement curve from Fig. 21 is used to generate a focused beam in the far field. The beam-steering radiation pattern for several beam directions at the center, lower, and higher frequency of bandwidth in both E-plane and H-plane is presented in Fig. 23, Fig. 24, and Fig. 25, respectively. As for the center frequency in the E-plane, the maximum measured gain occurs at around "θ=20˚" with 14.35 dBi realized gain at 27.5 GHz, and the main beam can be steered from -10˚ to -50˚ with 3-dB gain drop from the maximum. The 3-dB beam-scanning range in the H-plane is ±50˚ where the gain reduces from 13.65 dB to 10.5 dB. The pattern for the other two frequencies shows an approximate 3-dB bandwidth of 1.5 GHz. The difference between measured and simulated gain is between 1.5 to 2 dB in the whole scanning range which is due to fabrication error and non-ideal free-space measurement of the phase-voltage curve.

The presented study leveraged the features of LC material and realized a fully reconfigurable and optically transparent RA. The measured results show a promising path toward new applications of millimeter waves. The method presented here can be also used to realize phased arrays and other types of reconfigurable electromagnetic structures. However, more investigation is needed to reduce the loss (increase efficiency) and increase the transparency of metal mesh in combination with LC material. Also, to fully exploit the transparency of liquid crystal, there is a need to develop new types of LC material that are optimized for both RF frequency and optics so that the transmission magnitude of light in LC material can be independent of wavelength.

The analysis presented here is necessary to know what the effect of non-uniform LC distribution is in the presence of metallic mesh. The discretization error has been eliminated with our proposed method. Furthermore, it should be noticed that the final effect of this error can be even much higher than that in this paper, which depends on LC thickness, frequency, the sharpness of resonance, the unit cell pattern, etc. Therefore, before designing the transparent antenna, the error and effective permittivity should be estimated.

VII. CONCLUSION

This study presented a method to realize an optically transparent beam-steering solution for the millimeter-wave application. A metal mesh is used to realize transparent conductive layers. Since the LC director distribution in the presence of metal mesh is unknown, the interaction of liquid crystal with the metal mesh is investigated in LCD Master 3D simulation software, and the RF performance of LC was modeled by discretizing the LC volume with different steps in CST Microwave Studio. Then the LC behavior is approximated with a new permittivity range. A 10×10 RA is designed and simulated with the help of the proposed method. To validate the simulation results, a transparent beam-steering RA is fabricated in the cleanroom, and fabrication methodologies are elaborated. The optical and RF performance of the prototype shows that the presented method and prototype is a promising technology for transparent 5G and 6G antenna applications. Although the loss is higher than conventional opaque LC unit cells or conventional transparent metal mesh with no LC, the RA still shows a good performance. Of course, more research is needed to address the drawbacks of this method, such as investigating different types of unitcell with lower loss, developing new types of LC with less loss tangent, optimizing the metal mesh structure, etc. which will be done in the future.

ACKNOWLEDGMENT

The Authors would like to thank SHINTECH OPTICS and

Mr. Mike Miyashita for providing the LCD Master 3D simulation software. Also, the authors want to thank Merck Electronics KGaA, Darmstadt, Germany for providing the GT7 Liquid Crystal.

REFERENCES

[1] S. V. Hum and J. Perruisseau-Carrier, “Reconfigurable reflectarrays and array lenses for dynamic antenna beam control: A review,” *IEEE Trans. Antennas Propag.*, vol. 62, no. 1, pp. 183–198, 2014, doi: 10.1109/TAP.2013.2287296.

[2] C. Kocia and S. V. Hum, “Design of an Optically Transparent Reflectarray for Solar Applications Using Indium Tin Oxide,” *IEEE Trans. Antennas Propag.*, vol. 64, no. 7, pp. 2884–2893, 2016, doi: 10.1109/TAP.2016.2555338.

[3] J. Peng, S. Qu, and M. Xia, “Optically Transparent Reflectarray Based on Indium Tin Oxide With Improved Efficiency,” vol. 68, no. 4, pp. 3289–3294, 2020.

[4] J. Hautcoeur *et al.*, “Transparency and electrical properties of meshed metal films,” *Thin Solid Films*, vol. 519, no. 11, pp. 3851–3858, 2011, doi: 10.1016/j.tsf.2011.01.262.

[5] S. H. Kang and C. W. Jung, “Transparent Patch Antenna Using Metal Mesh,” *IEEE Trans. Antennas Propag.*, vol. 66, no. 4, pp. 2095–2100, 2018, doi: 10.1109/TAP.2018.2804622.

[6] M. Kim *et al.*, “Antenna-on-Display Concept on an Extremely Thin Substrate for Sub-6 GHz Wireless Applications,” vol. 70, no. 7, pp. 5929–5934, 2022.

[7] D. Kitayama, Y. Hama, K. Goto, K. Miyachi, T. Motegi, and O. Kagaya, “Transparent dynamic metasurface for a visually unaffected reconfigurable intelligent surface: controlling transmission/reflection and making a window into an RF lens,” *Opt. Express*, vol. 29, no. 18, p. 29292, 2021, doi: 10.1364/oe.435648.

[8] G. Liu, M. R. Dehghani Kodnoeih, K. T. Pham, E. M. Cruz, D. González-Ovejero, and R. Sauleau, “A Millimeter-Wave Multibeam Transparent Transmitarray Antenna at Ka-Band,” *IEEE Antennas Wirel. Propag. Lett.*, vol. 18, no. 4, pp. 631–635, 2019, doi: 10.1109/LAWP.2019.2899925.

[9] X. Y. Li, D. Jiang, J. Liu, and M. S. Tong, “A Ka-Band Multilayer Beaming-Scanning Antenna Using Liquid Crystals,” *IEEE Antennas Wirel. Propag. Lett.*, vol. 21, no. 1, pp. 44–48, 2022, doi: 10.1109/LAWP.2021.3116661.

[10] D. Wang, E. Polat, H. Tesmer, R. Jakoby, and H. Maune, “A Compact and Fast × 4 Continuously Steerable Endfire Phased-Array Antenna Based on Liquid Crystal,” *IEEE Antennas Wirel. Propag. Lett.*, vol. 20, no. 10, pp. 1859–1862, 2021, doi: 10.1109/LAWP.2021.3096035.

[11] H. Kim, J. Kim, and J. Oh, “A Novel Systematic Design of High-Aperture-Efficiency 2D Beam-Scanning Liquid-Crystal Embedded Reflectarray Antenna for 6G FR3 and Radar Applications,” *IEEE Trans. Antennas Propag.*, vol. 70, no. 11, pp. 11194–11198, 2022, doi: 10.1109/TAP.2022.3209178.

[12] P. Aghabeyki, Y. Cai, G. Deng, Z. H. Tan, and S. Zhang, “A Dual-Polarized Reconfigurable Reflectarray with A Thin Liquid Crystal Layer and 2D Beam Scanning,” *IEEE Trans. Antennas Propag.*, vol. 71, no. 4, pp. 3282–3293, 2023, doi: 10.1109/TAP.2023.3240853.

[13] Z. J. Silva, “OPTICALLY TRANSPARENT ANTENNAS FOR MULTI-MODAL SENSING,” Georgia Institute of Technology, 2019.

[14] R. H. Chen, *Liquid Crystal: DisplaysFundamental Physics and Technology*. New Jersey: John Wiley & Sons, 2011.

[15] R. James, F. A. Fernández, S. E. Day, S. Bulja, and D. Mirshekar-Syahkal, “Accurate modeling for wideband characterization of nematic liquid crystals for microwave applications,” *IEEE Trans. Microw. Theory Tech.*, vol. 57, no. 12, pp. 3293–3297, 2009, doi: 10.1109/TMTT.2009.2033864.

[16] Z. Ge, T. X. Wu, R. Lu, X. Zhu, Q. Hong, and S. T. Wu, “Comprehensive Three-dimensional Dynamic Modeling of Liquid Crystal Devices Using Finite Element Method,” *IEEE Antennas Propag. Soc. AP-S Int. Symp.*, vol. 1, no. 2, p. 1777, 2006, doi: 10.1109/APS.2006.1710910.

[17] A. Alex-Amor *et al.*, “Analytical Approach of Director Tilting in Nematic Liquid Crystals for Electronically Tunable Devices,” *IEEE Access*, vol. 7, no. February, pp. 14883–14893, 2019, doi: 10.1109/ACCESS.2019.2894167.

[18] G. Perez-Palomino *et al.*, “Accurate and efficient modeling to calculate the voltage dependence of liquid crystal-based reflectarray cells,” *IEEE Trans. Antennas Propag.*, vol. 62, no. 5, pp. 2659–2668, 2014, doi: 10.1109/TAP.2014.2308521.

[19] W. Zhang, Y. Li, and Z. Zhang, “A Reconfigurable Reflectarray Antenna with an 8-μm-thick Layer of Liquid Crystal,” *IEEE Trans. Antennas Propag.*, no. c, pp. 1–1, 2021, doi: 10.1109/tap.2021.3125378.

[20] J. Yang *et al.*, “Reflective liquid crystal terahertz phase shifter with tuning range of over 360°,” *IET Microwaves, Antennas Propag.*, vol. 12, no. 9, pp. 1466–1469, 2018, doi: 10.1049/iet-map.2017.0898.

[21] G. Perez-Palomino *et al.*, “Design and experimental validation of liquid crystal-based reconfigurable reflectarray elements with improved bandwidth in F-band,” *IEEE Trans. Antennas Propag.*, vol. 61, no. 4, pp. 1704–1713, 2013, doi: 10.1109/TAP.2013.2242833.

[22] G. Perez-Palomino, J. A. Encinar, and M. Barba, “Accurate electromagnetic modeling of liquid crystal cells for reconfigurable reflectarrays,” *Proc. 5th Eur. Conf. Antennas Propagation, EUCAP 2011*, pp. 997–1001, 2011.

Peyman Aghabeyki (Graduate Student Member, IEEE) was born in Mazandaran Province, Iran in 1993. He received a BSc degree in electrical engineering from Nooshirvani University of Technology, Babol, Iran, in 2016 and an MSc in Telecommunication Engineering, Field and waves with a focus on SIW antennas from the Amirkabir University of Technology, Tehran, Iran in 2019. He is currently pursuing a Ph.D. degree in the Antennas, Propagation, and Millimeter-wave Systems (APMS) section, at the Department of Electronic Systems, Aalborg University, Aalborg, Denmark. His main research interests include Liquid Crystal-based Reflectarrays and antennas for millimeter-wave applications.

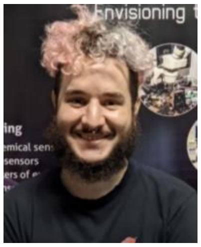

Pablo de la Rosa received a B.Sc. degree in telecommunication engineering from the Universidad Politécnica de Madrid (UPM), Madrid, Spain, in 2021, and an M.Sc. degree in photonics engineering from the Universidad Carlos III de Madrid (UC3M), Madrid, in 2022. He is currently pursuing a Ph.D. degree in intelligent reconfigurable surfaces based on liquid crystals with the Applied Electromagnetism Group (GEA), UPM. He conducted his bachelor’s thesis on the design of electronic drivers for liquid crystal devices, and his master’s thesis on manufacturing optical liquid crystal devices both at the CEMDATIC, UPM.

Manuel Caño-García received the M.Sc. degree in physics and the M.Sc. degree in electronic engineering from the University of Granada, Granada, Spain, in 2006 and 2013, respectively, the M.Sc. degree in nanotechnology from the Autonomous University of Madrid, Madrid, Spain, in 2014, and the international Ph.D. degree (summa cum laude) in photonics from the Technical University of Madrid (UPM), Madrid, in 2018, within the Spanish Official Grant (FPI 2014). He has been involved in three European projects and four Spanish national projects. He did a two-year post-doctoral stay at the International Iberian Nanotechnology Laboratory, Braga, Portugal, with the Marie Skłodowska-Curie Actions Scholarship and currently has a Distinguished Researcher Contract at the CEMDATIC Center, UPM, with the Beatriz Galindo Grant. His research revolves around the development of active photonics integrated circuits (PICs) with metamaterials or photonics crystals technologies for bio-sensing

Xabier Quintana is currently a Professor at the Technical University of Madrid (UPM), Madrid, Spain. He has been developing his activity at the Escuela Técnica Superior de Ingenieros (ETSI) de Telecomunicación, UPM, since 1993. He is the co-author of more than 50 international publications in scientific journals with an impact index. He has made more than 150 communications to international conferences. He is also the co-author of eight patents. His research interests include guided optical communications (anisotropic waveguides and unconventional fibers), unguided optical communications (atmospheric transmission and space), photonic applications of liquid crystals (displays, micro-displays, phase devices, tunable filters, and modal lenses), and organic electronics (OLEDs and organic photodetectors).

Robert Guirado received his B.S. and M.S. in Telecommunication Systems Engineering from Universitat Politècnica de Catalunya (Barcelona, Spain) in 2019 and 2021, respectively. Between February 2019 and August 2019, he was a visiting research student at the Georgia Institute of Technology. From September 2019 to January 2021, he worked as a research assistant at the NaNoNetworking Center in Catalonia. He conducted his Master's Thesis at IBM Research Zurich from February 2021 to July 2021. He is currently pursuing his Ph.D. degree on reconfigurable intelligent surfaces based on liquid crystals, funded by a “La Caixa” foundation fellowship.

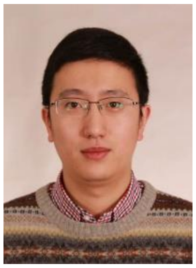

Shuai Zhang received a B.E. degree from the University of Electronic Science and Technology of China, Chengdu, China, in 2007 and a Ph.D. degree in electromagnetic engineering from the Royal Institute of Technology (KTH), Stockholm, Sweden, in 2013. In 2014, he joined Aalborg University, Denmark, where he currently works as Associate Professor and the head of the antenna research group with over 12 staff. In 2010 and 2011, he was a Visiting Researcher at Lund University, Sweden, and at Sony Mobile Communications AB, Sweden, respectively. He was also an external antenna specialist at Bang & Olufsen, Denmark from 2016-2017. He has supervised/co-supervised 7 Postdocs and 18 Ph.D. students. He has co-authored over 115 articles in well-reputed international journals and over 16 US or WO patents. His citations in Scopus are over 3700 with an H index of 29. His current research interests include millimeter-wave antennas for cellular communications, biological effects, metasurfaces, CubeSat antennas, Massive MIMO antennas, wireless sensors, and RFID antennas.

He is the Associate Editor for IEEE Antennas and Wireless Propagation Letters; Sensors; and IET Microwaves, Antennas, and Propagation. He is also a reviewer for all the top IEEE and IET journals in antenna areas, where he got the prize of “Top Reviewers in IEEE Transactions on Antennas and Propagation 2019-2020 and 2020-2021”. He is the General Co-Chair for iWAT2023 at Aalborg, Denmark, the Super Reviewer (previously known as Super TPC or Vice Chair) for IEEE APS 2020 and 2021, and the TPC for several top IEEE conferences. He is the recipient of “IEEE Antennas and Propagation Society Young Professional Ambassador” in 2022, where he gave a presentation for different IEEE Chapters on mm-wave mobile terminal antennas and massive MIMO base station antennas. He has also been intensively invited to international conferences and industry to give keynote/plenary speeches and presentations. He was invited to serve as a reviewer for the Icelandic Research Fund in 2019 and 2020. From 2019-2023, He is the Management Committee for EU COST Action CA18223 of SyMat, which mainly focuses on highly symmetrical periodic structures or metamaterials.